Kohli, Wolfson-Schwehr, Prigent, and Warren, 2021:
Oceanic transform fault seismicity and slip mode influenced by seawater infiltration,
Nature Geoscience, 14, 606-611, doi:10.1038/s41561-021-00778-1.

Oceanic transform fault seismicity and slip mode influenced by seawater infiltration

Arjun Kohli[1], Monica Wolfson-Schwehr[2], Cécile Prigent[3] and Jessica M. Warren[4]

[1]Stanford University Department of Geophysics

[2]Monterey Bay Aquarium Research Institute

[3]Université de Paris, Institut de physique du globe de Paris, CNRS

[4]University of Delaware Department of Earth Sciences

Corresponding Authors:

Arjun Kohli (ahkohli@stanford.edu), ORCID: 0000-0001-8798-5508

Jessica Warren (warrenj@udel.edu), ORCID: 0000-0002-4046-4200

Oceanic transform faults that offset mid-ocean ridges slip through earthquakes and aseismic creep. The mode of slip varies with depth and along strike, with some fault patches rupturing in large, quasi-periodic earthquakes at temperatures <600 °C, while others slip through creep and microearthquakes at temperatures up to 1000 °C in modeled thermal structure. Rocks from both fast- and slow-slipping transforms show evidence of interactions with seawater up to temperatures of at least 900 °C. Here we present a model for the mechanical structure of oceanic transform faults based on fault thermal structure and the impacts of hydration and metamorphic reactions on mantle rheology. Deep fluid circulation is accounted for in a modified friction-effective pressure law and in ductile flow laws for olivine

and serpentine. Incorporating observations of grain size reduction and hydrous mineralogy from high strain mylonites results in a broad temperature range over which brittle and ductile deformation can occur, 300-1000 °C. The ability of seawater to penetrate the fault determines whether slip is accommodated at depth by seismic asperities or by aseismic creep in weak, hydrous shear zones. Our results suggest that seawater infiltration controls the extent of seismicity and spatiotemporal variations in the mode of slip.

Global studies of seismicity[1–3] and deformation experiments on olivine[4] suggest that 600-700 °C is the thermal limit for earthquake nucleation on oceanic transform faults (OTFs). However, recent ocean bottom seismometer (OBS) deployments on fast- and intermediate-slipping transforms have located microearthquakes in the mantle at temperatures up to 1000 °C in modeled thermal structure[5–8]. The mode of slip is also observed to vary along-strike, with some fault patches hosting large, quasi-periodic earthquakes while others arrest the propagation of large ruptures and slip through intense swarms of deep microseismicity[5]. Rupture barrier zones show low seismic velocities and high V_p/V_s ratios indicating high porosity, which suggests a causal link between hydrologic properties and the seismogenic behavior of the lithosphere[9,10]. Earthquake cycle models demonstrate that increased dilatancy in these regions can account for observations of slow slip and the arrest of large ruptures, but does not explain variations in the vertical extent of microseismicity or along-strike variations in the mode of slip at temperatures >600-700 °C[11].

Deformed mantle rocks have been dredged from OTFs spanning a wide range of slip rates (Fig. 1a) and provide constraints on the conditions and mechanisms of fault slip. In particular, high-strain mylonites contain syn-deformational hydrous phases, signifying that fluids were present during ductile deformation[12,13]. Analysis of mylonites from ultra-slow slipping faults on the Southwest Indian Ridge (SWIR) indicates that fluids are derived from seawater and that fluid-rock interactions occur up to at least 900 °C. In this study, we use temperature constraints from the mylonites in combination with numerical models of fault thermal structure to construct a rheological profile of OTFs that incorporates deep seawater circulation and fluid-deformation feedbacks. We use this framework to explain OBS observations[5–8] of along-strike variations in the mode of slip and the extent of seismicity.

OTF Mylonites

Mantle mylonites have been dredged from numerous OTFs (Fig. 1a). The presence of syn-deformational hydrous phases in fine-grained shear zones within mylonites indicates that they formed under hydrous conditions (Fig. 1c). We use these hydrous phases to classify mylonites in terms of the temperature of deformation[13]. Low temperature (LT) mylonites contain amphibole, chlorite, and serpentine. Medium temperature (MT) mylonites contain both amphibole and chlorite. High temperature (HT) mylonites contain amphibole as the only hydrous phase. LT to HT mylonites with similar characteristics (very fine grain size compared to abyssal peridotites, syn-deformational hydrous phases) have been recovered from the fastest- (Garrett) and slowest-slipping (Shaka) transform faults (Supplementary Information Table 1). The high chlorine content of hydrous minerals in SWIR mylonites (up to 1 wt%) indicates that the fluid source was seawater (Fig. 1e).

The temperature during deformation of LT/MT/HT mylonites can be inferred from the stability fields of hydrous minerals. However, the depth of deformation cannot be directly estimated from mineralogy, as none of the mineral compositions are pressure-sensitive. We therefore use fault thermal models to convert temperature constraints into pressure/depth on the fault (Fig. 2a-b). Three-dimensional thermal models were solved for the flow field and thermal structure of the Shaka and Gofar transform faults (see Methods). We compare geotherms from the center of each fault with the experimentally-derived upper stability limits of hydrous minerals[14–17] and thermometry estimated based on orthopyroxene composition (Fig. 2c). We designate LT/MT/HT mylonite regions based on hydrous mineralogy and use these regions as the bounds on the pressure-temperature conditions of deformation.

Fault rheology and fluid-deformation feedbacks

The mechanisms governing ductile deformation in OTF mylonites and their protolith can be interpreted from the mylonite microstructures[12]. Prior to deformation in the fault zone, the mantle protolith is assumed to be coarse-grained peridotite formed by melt extraction within the asthenosphere (Fig. 3a inset). This starting point corresponds to the pressure/depth at which the fault is at the mantle potential temperature in the thermal models (see Methods). We use the grain size and pressure-temperature conditions to construct deformation mechanism maps for the protolith on Shaka and Gofar using olivine flow laws[18–20] (Extended Data Figs. 1, 2). Flow law equations and parameters are provided in Extended Data Table 2. For both faults, the protolith is expected to deform by a combination of dislocation creep and grain boundary sliding at strain rates of ~10^{-9}-10^{-11} s^{-1}.

Once fluids are introduced into the fault zone, weak, fine-grained shear zones can form via a positive feedback loop. The presence of fluids weakens olivine, increasing strain rate and decreasing grain size[21–24]. Fluids are drawn into rapidly-deforming zones[25], where the formation of hydrous phases further weakens olivine through grain size reduction due to phase boundary pinning[12,26]. The formation of mylonites from the mantle protolith represents a reduction in grain size of 2-3 orders of magnitude. This process results in a change in the olivine deformation mechanism from grain size-insensitive to grain size-sensitive creep[12], thereby strengthening the fluid-deformation feedbacks.

Using the pressure-temperature conditions estimated for the mylonites, we construct deformation mechanism maps for the LT/MT/HT regions using flow laws for olivine and serpentine (Extended Data Figs. 1, 2). Amphibole and chlorite flow laws have not been developed. While laboratory tests[27] and analyses of exhumed mantle shear zones[28] suggest that amphibole is stronger than olivine, in OTF mylonites, the proportion of amphibole is inversely correlated with olivine grain size[12,13]. This indicates that the rheological impact of amphibole is to weaken peridotite by pinning olivine grain boundaries. At the average grain size of the fine-grained zones within the mylonites (1-10 μm), olivine deformation occurs entirely within the diffusion creep field and serpentine deforms by dislocation creep[29]. Assuming iso-stress deformation[30], the estimated strain rates for the mylonites span over ten orders of magnitude (~10^{-5}-10^{-17} s^{-1}; Extended Data Fig. 3).

Brittle-ductile deformation and seawater infiltration

To estimate the depth extent of brittle deformation and seawater infiltration, we calculate strength-depth profiles for Shaka and Gofar using the modeled geotherms, measured grain sizes, and estimated strain rates (Fig. 3). For each flow law, we consider the transition from brittle (pressure-dependent) to ductile (temperature-dependent) behavior as the depth at which the flow law intersects the modified friction-effective stress line (Extended Data Fig. 4, Methods). The protolith has an olivine grain size of ~1-5 mm and deforms by a combination of dislocation creep and grain boundary sliding (Extended Data Figs. 1, 2). Under these conditions, olivine transitions from brittle to ductile behavior at 22-24 km on Shaka and 6-7 km on Gofar. This represents the base of the brittle-ductile zone and corresponds to a temperature range of ~900-1000 °C.

While our rheological model indicates that brittle deformation of olivine is possible at 1000°C at slow (interseismic) strain rates, the amphibole minerals that form during hydration of the HT mylonites are only stable at lower temperatures (Fig. 2c). Therefore, the stability limit of amphibole represents a minimum estimate for the depth limit of seawater-mantle interactions on OTFs. Hydrothermal fluids may percolate deeper, down to the base of the brittle-ductile transition, but leave no mineralogical signature as no hydrous phases associated with peridotite are stable at >900 °C. The Shaka mylonites contain healed fractures filled with fluid inclusions within porphyroclasts, which suggests that hydration occurred at temperatures beyond amphibole stability in the coarse-grained protolith[12].

The formation of hydrous peridotite mylonites results in a wide temperature range over which brittle and ductile deformation are coeval. The base of this zone is defined by olivine in the HT mylonites, which undergoes a transition from brittle to ductile behavior at ~700-900 °C. The shallow extent of the brittle-ductile zone is defined by the rheology of serpentine, the weakest phase in the LT mylonites[29]. Serpentine is frictionally weak compared to olivine (Byerlee's law)[31–33]. As its frictional strength depends on a variety of factors, we use a depth-dependent friction coefficient ranging from 0.1-0.6 based on values determined in experimental studies[31–33] (see

Supplementary Information). The intersection of the serpentine flow law with the bounds on frictional strength yields a temperature range of ~300-400 °C. The depth range of the brittle-ductile transition zone where LT to HT mylonites can form is 4-22 km on Shaka and 1-5 km on Gofar.

Controls on the extent of seismicity on OTFs

The best geophysical constraints on the depth extent of brittle deformation on OTFs are earthquakes recorded during OBS deployments on Gofar/Discovery/Quebrada on the fast-spreading EPR[5,6,9] and Blanco on the intermediate-spreading Juan de Fuca Ridge[8] (Fig. 1a). These studies show along-strike variations in the maximum depth of seismicity. On some fault patches earthquakes are limited to depths corresponding to <600-700 °C in modeled thermal structure, while on others seismicity extends into the mantle up to 1000 °C[6]. The thermal limit of seismicity determined in OBS studies is consistent with our estimates of the temperature of the brittle-ductile transition from the rheology of coarse-grained peridotite and mantle mylonites from Shaka. LT to HT mylonites from Garrett transform fault (Fig. 1a), show nearly identical microstructures to the Shaka mylonites, indicating that the same fluid-deformation feedbacks that occur on slow-slipping transforms also take place on fast-slipping transforms[34,35].

Our calculations demonstrate that along-strike differences in mantle hydration can result in spatiotemporal variations in the mode of slip on OTFs. Progressive hydration and the formation of weak mantle mylonites increases the contribution of aseismic creep, decreasing seismic coupling in the mantle. OBS observations of along-strike variations in the mode of slip on fast- and intermediate-slipping transform faults[5,7,36,37] support this model. On asperity patches, where large, quasi-periodic ruptures occur, seismicity is limited to the crust, while in the barrier regions, where large ruptures stop, microseismicity extends into the mantle[5,6]. Seismological studies of the Gofar OBS dataset show low P-wave velocities and stress drops in the barrier regions, which is attributed to enhanced hydrothermal circulation and alteration resulting from fault zone damage[9,38]. Modeling of earthquake cycles on Gofar shows that enhanced dilatancy in damage zones results in aseismic transients and rupture arrest in the seismogenic zone[11]. This explains along-strike variations in the mode of slip in the shallow part of the fault, but cannot explain differences in the depth extent of seismicity between the asperity and barrier zones, as dilatancy is inhibited at higher pressures.

Based on our rheological model, we propose that barrier regions on OTFs correspond to sections of the fault where hydrated mylonite shear zones are not pervasive at depth (Fig. 4). These regions instead contain relatively coarse-grained peridotite, which is expected to sustain brittle behavior at greater pressure-temperature conditions compared to mylonites. This model is supported by our observation that coarse-grained peridotites recovered from SWIR transform faults exhibit greater fracture density and hydrothermal alteration compared to mylonites[12,13], consistent with geophysical interpretations of the Gofar barrier region[10]. The Gofar OBS data shows that seismicity on asperity regions is limited to temperatures <600-700 °C[5], in agreement with our estimate of the thermal limit of brittle deformation in regions where MT/HT mylonites have formed (Fig. 3b). This implies that asperity patches are underlain by weak, hydrated shear zones where slip is accommodated by relatively rapid, aseismic creep. Accumulated aseismic slip in these shear zones may be responsible for loading the shallow portion of the asperity regions, as well as the deep portion of adjacent coarser-grained regions, possibly driving large ruptures in the asperity regions and deep microseismicity in the barrier regions.

Our results demonstrate that vertical and along-strike variations in the extent of seismicity on OTFs can be explained by the impacts of deep seawater circulation on effective stress and fault rheology. The formation of hydrous mantle mylonites over a broad temperature range (300-900 °C) allows slip to be accommodated by aseismic creep. While variations in dilatancy can explain the slip dynamics of seismic and aseismic patches in the crust[11], the formation of these patches and their extent within the mantle are determined by seawater-rock interactions. Therefore, a new generation of OTF models is needed that incorporate constraints on seawater infiltration from fault rocks, as well as feedbacks between hydration, thermal structure, and fault rheology. Allowing the multi-modal slip behavior observed on OTFs[36–38] to evolve dynamically over time will further our understanding of how fluid flow in fault zones contributes to spatiotemporal variations in the slip behavior of plate interfaces.

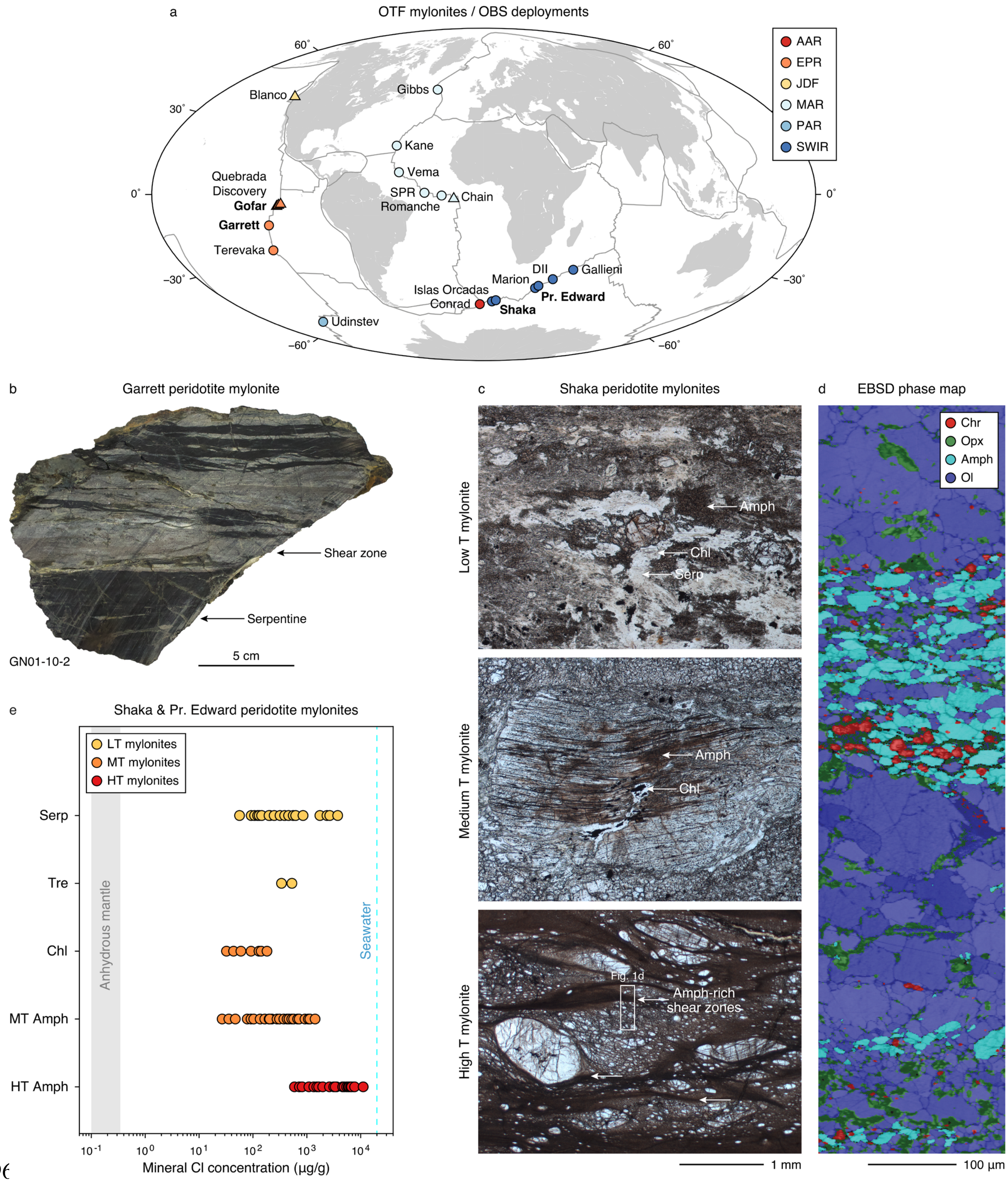
a
OTF mylonites / OBS deployments
AAR
EPR
JDF
MAR
PAR
SWIR
Blanco
Gibbs
Kane
Vema
SPR
Romanche
Chain
Quebrada
Discovery
Gofar
Garrett
Terevaka
Udinstev
Islas Orcadas
Conrad
Shaka
Marion
DII
Gallieni
Pr. Edward
b
Garrett peridotite mylonite
Shear zone
Serpentine
GN01-10-2
5 cm
c
Shaka peridotite mylonites
Low T mylonite
Medium T mylonite
High T mylonite
Amph
Chl
Serp
Fig. 1d
Amph-rich shear zones
1 mm
d
EBSD phase map
Chr
Opx
Amph
Ol
100 µm
e
Shaka & Pr. Edward peridotite mylonites
LT mylonites
MT mylonites
HT mylonites
Serp
Tre
Chl
MT Amph
HT Amph
Anhydrous mantle
Seawater
Mineral Cl concentration (µg/g)

196

Fig. 1 | Map and microstructures of oceanic transform fault mylonites. (a) Global map of oceanic transform faults where mylonites have been recovered (circles) and ocean-bottom seismometers have been deployed (triangles). Bolded faults are discussed in the main text. (b) Serpentinized peridotite mylonite from the fast-slipping Garrett transform fault. (c) Photomicrographs (plane polarized light) of high, medium, and low temperature mylonites from the slow-slipping Shaka transform fault. Amph - amphibole; Chl - chlorite; Serp - serpentine. (d) Electron backscatter diffraction phase map of fine-grained, amphibole-rich bands within a high temperature mylonite. (e) Chlorine concentrations in hydrous minerals in Shaka and Pr. Edward mylonites.

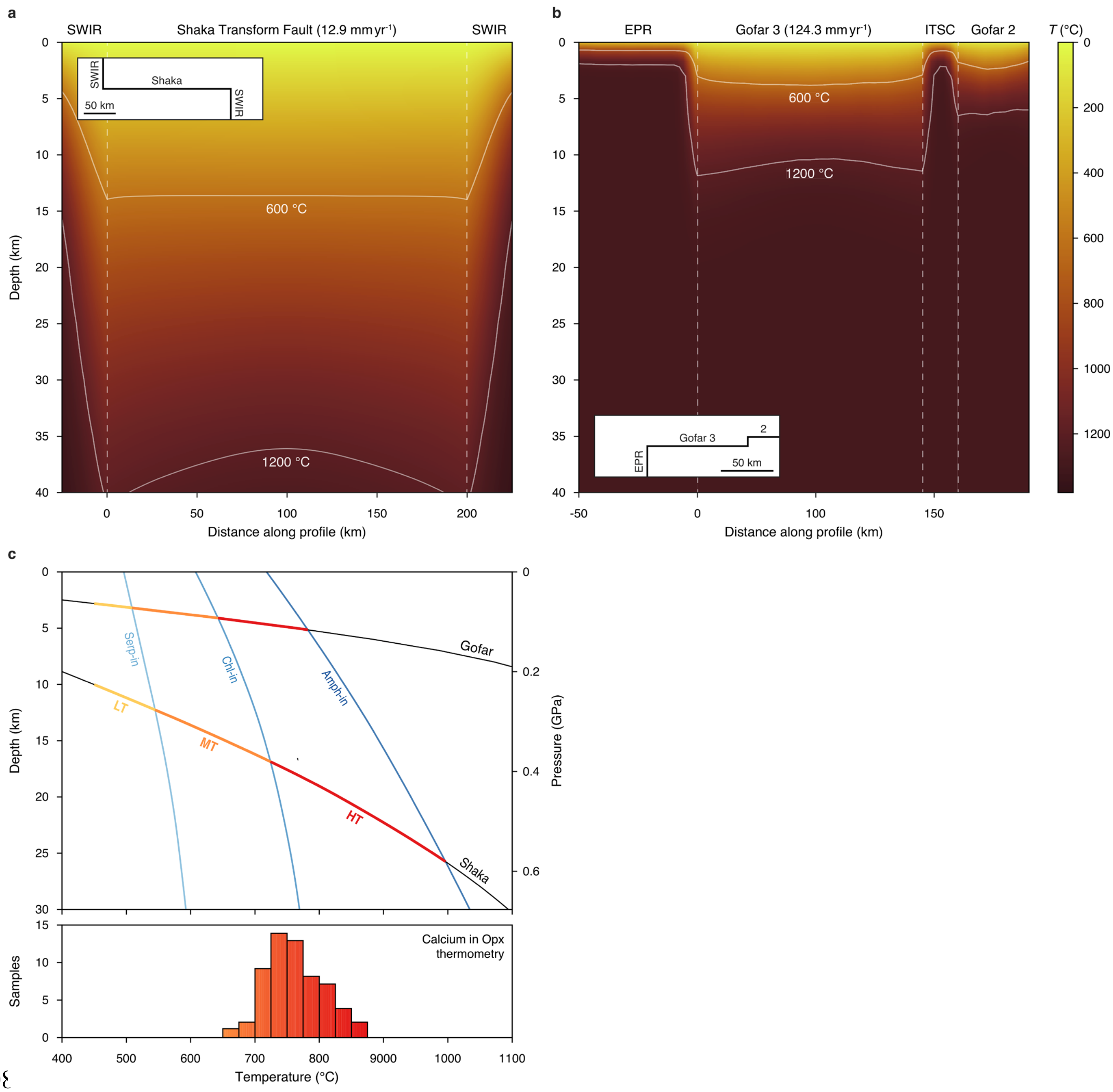

Fig. 2 | Thermal models and hydrous mineralogy of oceanic transform faults. (a) Shaka (b) Gofar segments 2 and 3. Profiles run parallel to the ridge-fault-ridge system (insets). See Extended Data Table 1 for model parameters. (c) (top) The intersection of fault center geotherms with the hydrous mineral stability limits for amphibole (Amph), chlorite (Chl), and serpentine (Serp), that phases that distinguish low, medium, and high temperature (LT/MT/HT) mylonites. (bottom) Mineral thermometry calculations ($T_{Ca\ in\ Opx}$) constrain the low temperature limit of ductile recrystallization in SWIR mylonites[13].

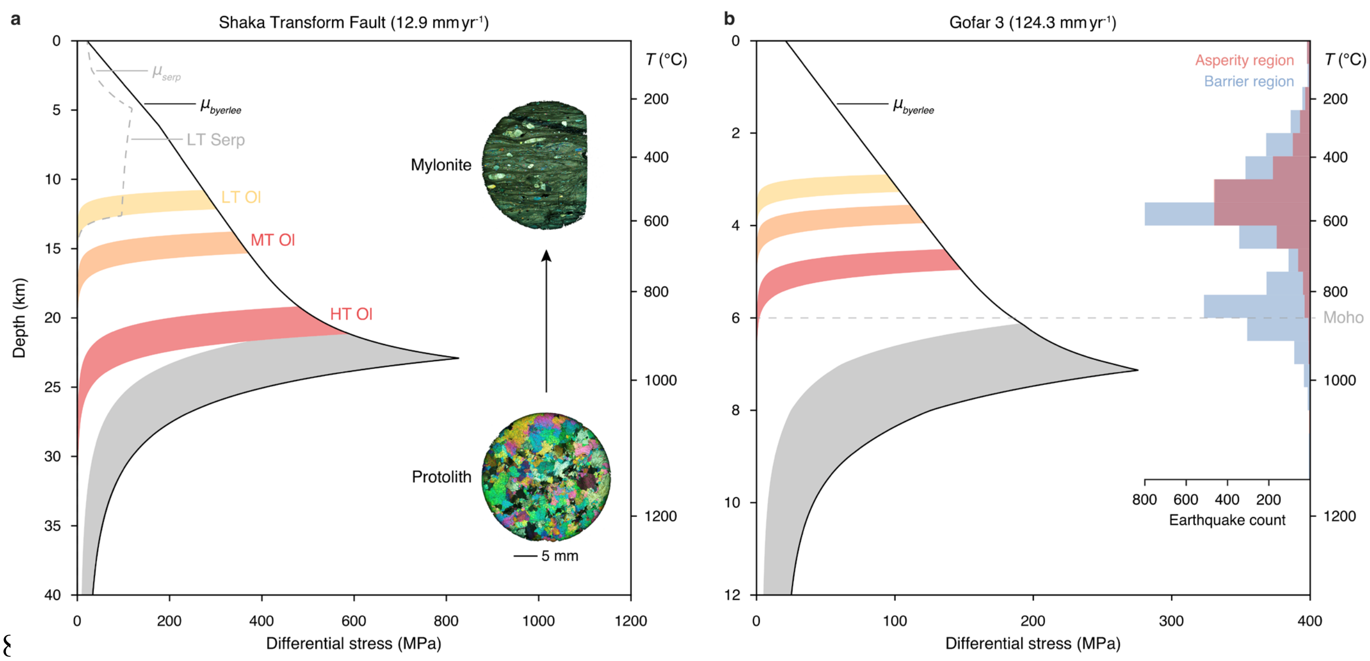

Fig. 3 | Strength-depth profiles for slow- and fast-slipping OTFs. The intersection of each flow law with the friction lines represents the transition from brittle to ductile behavior. The lines $\mu_{byerlee}$ and μ_{serp} represent the frictional strengths of olivine and serpentine (see Methods). Each colored region corresponds to flow laws calculated over the range of estimate deformation conditions (Supplementary Information Table 5). (a) Shaka. Insets show characteristic protolith and mylonite microstructures. (b) Gofar segment 3. Histograms show the earthquake count in the asperity and barrier regions from the 2008 OBS experiment[5,9]. The Moho depth was determined by seismic tomography[6].

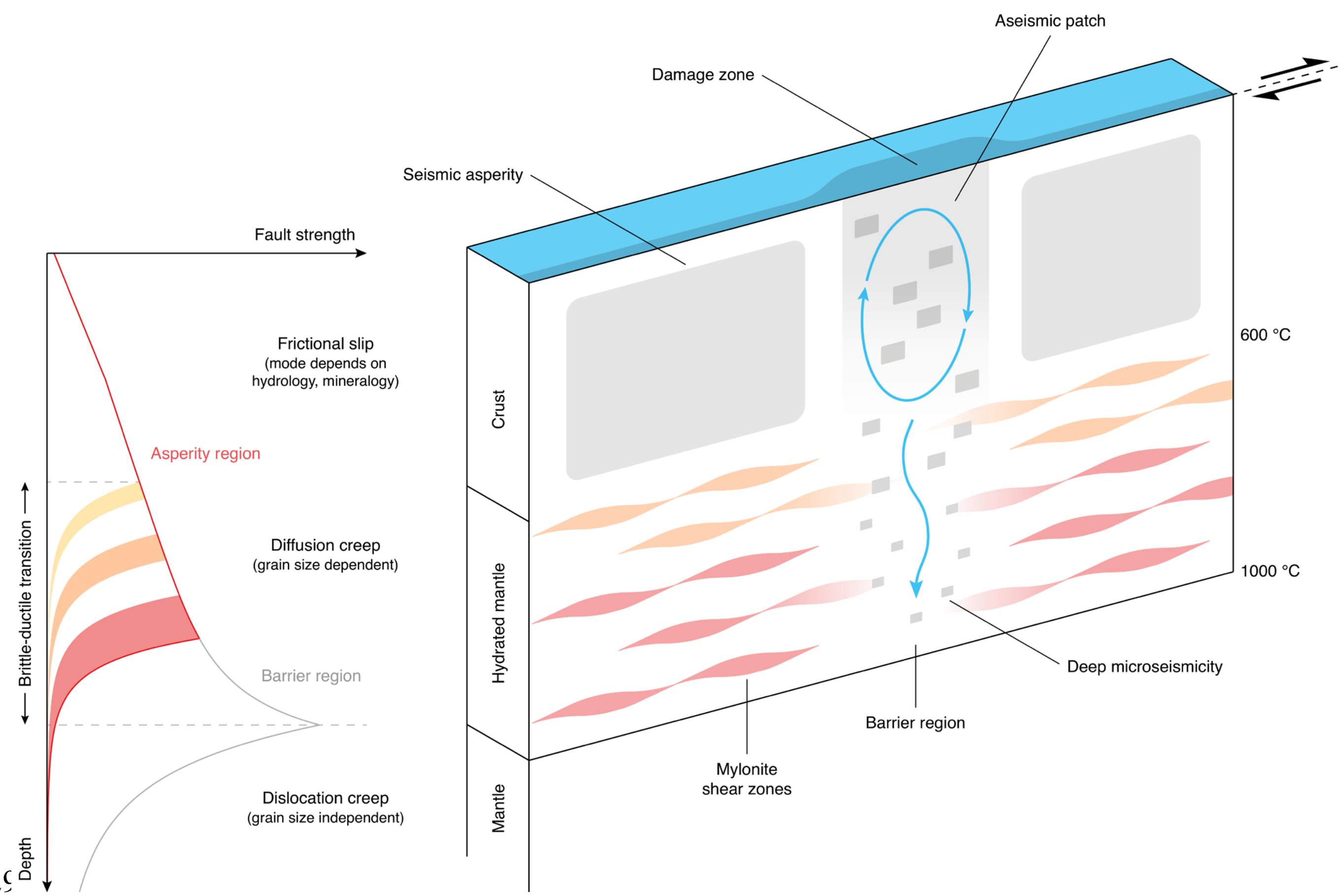

Fig. 4 | Vertical and along-strike variations in seismicity on OTFs. Fully coupled seismic asperity patches (grey boxes) are limited in vertical extent by the 600-700 °C isotherm, below which weak mylonite shear zones (colored bands) can form. Asperity regions are separated by barrier regions that slip through aseismic creep and microearthquakes that extend into the mantle lithosphere. Over time, these rupture barriers may become asperity patches as mantle rheology and mineralogy evolve with progressive hydration and strain.

Data Availability

OTF mylonite and OBS deployment locations are provided in the Supplementary Information. OTF mylonite compositional data is available at EarthChemLibrary (http://www.earthchem.org/library) at the identifier doi:10.1594/IEDA/111356. The Gofar seismic data is available from the IRIS Data Management Center (https://www.fdsn.org/networks/detail/ZD_2007/).

Code Availability

The codes used to generate the thermal models, deformation mechanism maps, and strength-depth profiles can be accessed at https://github.com/ahkohli/OTFs.

References

1. Wiens, D. A. & Stein, S. Age dependence of oceanic intraplate seismicity and implications for lithospheric evolution. *J. Geophys. Res.* **88**, 6455–6468 (1983).
2. Chen, W.-P. & Molnar, P. Focal depths of intracontinental and intraplate earthquakes and their implications for the thermal and mechanical properties of the lithosphere. *J. Geophys. Res.* **88**, 4183–4214 (1983).
3. Abercrombie, R. E. & Ekström, G. Earthquake slip on oceanic transform faults. *Nature* **410**, 74–77 (2001).
4. Boettcher, M. S., Hirth, G. & Evans, B. Olivine friction at the base of oceanic seismogenic zones. *J. Geophys. Res.* **112**, 1–13 (2007).
5. McGuire, J. J. *et al.* Variations in earthquake rupture properties along the Gofar transform fault, East Pacific Rise. *Nat. Geosci.* **5**, 336–341 (2012).

6. Roland, E., Lizarralde, D., McGuire, J. J. & Collins, J. A. Seismic velocity constraints on the material properties that control earthquake behavior at the Quebrada-Discovery-Gofar transform faults, East Pacific Rise. *J. Geophys. Res.* **117**, 1–27 (2012).
7. Wolfson-Schwehr, M., Boettcher, M. S., McGuire, J. J. & Collins, J. A. The relationship between seismicity and fault structure on the Discovery transform fault, East Pacific Rise. *Geochemistry, Geophys. Geosystems* **15**, 3698–3712 (2014).
8. Kuna, V. M., Nábělek, J. L. & Braunmiller, J. Mode of slip and crust–mantle interaction at oceanic transform faults. *Nat. Geosci.* **12**, 138–142 (2019).
9. Froment, B. *et al.* Imaging along-strike variations in mechanical propeties of the Gofar transform fault, East Pacific Rise. *J. Geophys. Res. Solid Earth* **119**, 7175–7194 (2014).
10. Guo, H., Zhang, H. & Froment, B. Structural control on earthquake behaviors revealed by high-resolution Vp/Vs imaging along the Gofar transform fault, East Pacific Rise. *Earth Planet. Sci. Lett.* **499**, 243–255 (2018).
11. Liu, Y., McGuire, J. J. & Behn, M. D. Aseismic transient slip on the Gofar transform fault, East Pacific Rise. *Proc. Natl. Acad. Sci.* **117**, 10188–10194 (2020).
12. Kohli, A. H. & Warren, J. M. Evidence for a deep hydrologic cycle on oceanic transform faults. *J. Geophys. Res. Solid Earth* **125**, 1–23 (2020).
13. Prigent, C., Warren, J. M., Kohli, A. H. & Teyssier, C. Fracture-mediated deep seawater flow and mantle hydration on oceanic transform faults. *Earth Planet. Sci. Lett.* **532**, 1–13 (2020).
14. Connolly, J. A. D. The geodynamic equation of state: What and how. *Geochemistry, Geophys. Geosystems* **10**, (2009).
15. Guillot, S., Schwartz, S., Reynard, B., Agard, P. & Prigent, C. Tectonic significance of

serpentinites. *Tectonophysics* **646**, 1–19 (2015).

16. Fumagalli, P., Zanchetta, S. & Poli, S. Alkali in phlogopite and amphibole and their effects on phase relations in metasomatized peridotites: A high-pressure study. *Contrib. to Mineral. Petrol.* **158**, 723–737 (2009).
17. Chernosky, Joseph V. Jr., Berman, Robert G., J. & Jenkins, D. M. The stability of tremolite: New experimental data and a thermodynamic assessment. *Am. Mineral.* **83**, 726–738 (1998).
18. Hirth, G. & Kohlstedt, D. Rheology of the upper mantle wedge: a view from the experimentalists. in *Inside the Subduction Factory* 83–105 (2003).
19. Hansen, L. N., Zimmerman, M. E. & Kohlstedt, D. L. Grain boundary sliding in San Carlos olivine: Flow law parameters and crystallographic-preferred orientation. *J. Geophys. Res. Solid Earth* **116**, 1–16 (2011).
20. Ohuchi, T. *et al.* Dislocation-accommodated grain boundary sliding as the major deformation mechanism of olivine in the Earth's upper mantle. *Sci. Adv.* **1**, 1–10 (2015).
21. Carter, N. L. & Avé Lallemant, H. G. High temperature flow of dunite and peridotite. *Geol. Soc. Am. Bull.* **81**, 2181–2202 (1970).
22. Karato, S.-I., Paterson, M. & Fitzgerald, D. Rheology of synthetic olivine aggregates: Influence of grain size and water. *J. Geophys. Res.* **91**, 8151–8176 (1986).
23. Chopra, P. N. & Paterson, M. S. The experimental deformation of dunite. *Tectonophysics* **78**, 453–473 (1981).
24. Hirth, G. & Kohlstedt, D. L. Water in the oceanic upper mantle: implications for rheology, melt extraction and the evolution of the lithosphere. *Earth Planet. Sci. Lett.* **144**, 93–108 (1996).

25. Fusseis, F., Regenauer-Lieb, K., Liu, J., Hough, R. M. & De Carlo, F. Creep cavitation can establish a dynamic granular fluid pump in ductile shear zones. *Nature* **459**, 974–977 (2009).
26. Précigout, J., Prigent, C., Palasse, L. & Pochon, A. Water pumping in mantle shear zones. *Nat. Commun.* **8**, 1–10 (2017).
27. Getsinger, A. J. & Hirth, G. Amphibole fabric formation during diffusion creep and the rheology of shear zones. *Geology* **42**, 535–538 (2014).
28. Tommasi, A., Langone, A., Padrón-Navarta, J. A., Zanetti, A. & Vauchez, A. Hydrous melts weaken the mantle, crystallization of pargasite and phlogopite does not: Insights from a petrostructural study of the Finero peridotites, southern Alps. *Earth Planet. Sci. Lett.* **477**, 59–72 (2017).
29. Hilairet, N., Reynard, B., Wang, Y., Daniel, I., Merkel, S., Nishiyama, N. and Petitgirard, S. High-pressure creep of serpentine, interseismic deformation, and initiation of subduction. *Science (80-.).* **318**, 1910–1913 (2007).
30. Platt, J. P. & Behr, W. M. Grain size evolution in ductile shear zones: Implications for strain localization and the strength of the lithosphere. *J. Struct. Geol.* **33**, 537–550 (2011).
31. Reinen, L. A., Weeks, J. D. & Tullis, T. E. The frictional behavior of lizardite and antigorite serpentinites: Experiments, constitutive models, and implications for natural faults. *Pure Appl. Geophys.* **143**, 317–358 (1994).
32. Moore, D. E., Lockner, D. A., Ma, S., Summers, R. & Byerlee, J. D. Strengths of serpentinite gouges at elevated temperatures. *J. Geophys. Res. Solid Earth* **102**, 14787–14801 (1997).
33. Moore, D. E. & Lockner, D. A. Frictional strengths of talc-serpentine and talc-quartz

mixtures. *J. Geophys. Res.* **116**, 1–17 (2011).

34. Cannat, M., Bideau, D. & Hébert, R. Plastic deformation and magmatic impregnation in serpentinized ultramafic rocks from the Garrett transform fault (East Pacific Rise). *Earth Planet. Sci. Lett.* **101**, 216–232 (1990).

35. Constantin, M. Gabbroic intrusions and magmatic metasomatism in harzburgites from the Garrett transform fault: Implications for the nature of the mantle-crust transition at fast-spreading ridges. *Contrib. to Mineral. Petrol.* **136**, 111–130 (1999).

36. Aderhold, K. & Abercrombie, R. E. The 2015 Mw 7.1 earthquake on the Charlie-Gibbs transform fault: Repeating earthquakes and multimodal slip on a slow oceanic transform. *Geophys. Res. Lett.* **43**, 6119–6128 (2016).

37. Wolfson-Schwehr, M. & Boettcher, M. S. Global characteristics of oceanic transform fault structure and seismicity. in *Transform Plate Boundaries and Fracture Zones* 21–59 (Elsevier, 2019).

38. Moyer, P. A., Boettcher, M. S., McGuire, J. J. & Collins, J. A. Spatial and temporal variations in earthquake stress drop on Gofar Transform Fault, East Pacific Rise: Implications for fault strength. *J. Geophys. Res. Solid Earth* **123**, 7722–7740 (2018).

39. Dalton, C. A., Langmuir, C. H. & Gale, A. Geophysical and geochemical evidence for deep temperature variations beneath mid-ocean ridges. *Science (80-.).* **344**, 80–83 (2014).

40. Behn, M. D., Boettcher, M. S. & Hirth, G. Thermal structure of oceanic transform faults. *Geology* **35**, 307–310 (2007).

41. Mei, S., Suzuki, A. M., Kohlstedt, D. L., Dixon, N. A. & Durham, W. B. Experimental constraints on the strength of the lithospheric mantle. *J. Geophys. Res. Solid Earth* **115**, 1–9 (2010).

42. Katayama, I. & Karato, S. Low-temperature, high-stress deformation of olivine under water-saturated conditions. *Phys. Earth Planet. Inter.* **168**, 125–133 (2008).

43. Bell, D. R., Rossman, G. R., Maldener, J., Endisch, D. & Rauch, F. Hydroxide in olivine: A quantitative determination of the absolute amount and calibration of the IR spectrum. *J. Geophys. Res. Solid Earth* **108**, 1–9 (2003).

Corresponding Authors

Please direct all correspondence to Arjun Kohli (ahkohli@stanford.edu) and Jessica Warren (warrenj@udel.edu).

Acknowledgements

We thank C. Teyssier, M. D'Errico, K. Kumamoto, L. Hansen, M. Boettcher, M. Behn, J. McGuire and G. Hirth for helpful discussions. J. McGuire provided the earthquake catalog from the Gofar OBS data. This work was supported by a NSF Graduate Research Fellowship to A. Kohli and NSF grants EAR-1347696, EAR- 1619880, and OCE-1832868 to J.M. Warren.

Author Contributions

A.K., C.P. and J.M.W. performed analyses of the mylonite samples. M.W-S. designed the thermal models. C.P. conducted the geochemical measurements. A.K. performed the rheology calculations. All authors discussed the results and contributed to writing the manuscript.

Competing Interests

The authors declare no competing interests related to this manuscript.

Methods

Thermal model. Thermal models were constructed using the finite element software package COMSOL Multiphysics (v.4.2a). In the models, ductile deformation follows a viscoplastic, temperature-dependent flow law, which has the form:

$$\dot{\varepsilon} = A\sigma^{n}e^{-E/RT} \tag{1}$$

where strain rate ($\dot{\varepsilon}$) is a function of the pre-exponential constant (A), differential stress (σ), stress exponent (n), activation energy (E), molar gas constant (R), and temperature (T).

Brittle deformation follows Byerlee's Law[44], where the maximum shear stress (τ_{max}) is a function of the friction coefficient (μ), normal stress (σ_n), and cohesive strength (τ_0):

$$\tau_{max} = \mu\sigma_n + \tau_0 \tag{2}$$

The inclusion of a temperature-dependent viscosity and a frictional failure law causes enhanced upwelling below the transform fault compared to thermal models that do not incorporate deformation[3,45]. This results in a warmer thermal structure overall, although the isotherms do not converge upwards when approaching the ridge axis, which creates a lower thermal gradient near the ridge[40]. The estimated mantle potential temperature for Shaka is 1380 °C[39], which is relatively high due to the passage of the Bouvet mantle plume[46]. For Gofar, the mantle potential temperature is assumed to be slightly lower, 1300 °C[40]. Values for thermal model parameters are provided in Extended Data Table 1. The ridge and fault geometry in the models is based on bathymetry data. Shaka is modeled as a single, 200-km long segment, while Gofar is discretized into 3 fault segments separated by small spreading ridges[6].

The ductile rheology is a dislocation creep flow law for dry olivine[18], which is grain size insensitive. The fine-grained layers of the Shaka mylonites are predicted to deform by wet diffusion creep (which is grain size sensitive), however the model is not currently designed to allow for the ductile flow law to vary spatially or temporally. The thermal model also does not account for deep hydrothermal circulation. The amount of cooling due to shallow hydrothermal circulation results in ~1-2 km deepening in the thermal structure[47], so extending fluid infiltration would further deepen (cool) the thermal structure. Grain size sensitive creep and enhanced hydrothermal circulation should be incorporated in future models in order to more accurately reflect the conditions of mylonite deformation. In addition, while secondary phases (pyroxene, amphibole) are important to mylonite deformation[12], our calculations only consider a pure olivine system. At present, flow laws for olivine-pyroxene or olivine-amphibole systems at mantle compositions are not available, though experiments have been conducted for more Fe-rich olivine-pyroxene mixtures[48]. As the extrapolation of this flow law to mantle compositions is unknown, the pure olivine flow law remains the best option for assessing the impacts of strain localization and hydration on fault rheology. However, our observation that the presence of hydrous phases weakens peridotite[12,13] suggests that the brittle-ductile transition may be shallower than predicted by olivine flow laws.

Strength-depth profiles. Brittle deformation is represented by frictional equilibrium for transform faults[49], in which the strength of the lithosphere is the differential stress.

$$\left(\sigma_1-\sigma_3\right)=\mu'(\sigma_n-P_f)+\tau_0 \tag{3}$$

σ_n is the fault normal stress, P_f is the pore fluid pressure and τ_0 is cohesion. The parameter μ' represents the minimum stress conditions to initiate fault slip, given a coefficient of friction, μ.

$$\mu' = 2\mu / (\mu^2 + 1)^{1/2} \tag{4}$$

The effective overburden pressure, σ_v, with depth, z, is given by:

$$\sigma_v = \rho g z(1-\lambda) \tag{5}$$

in which ρ is density, g is acceleration due to gravity, and λ is the ratio of the pore fluid pressure, P_f, to the overburden. Following previous studies[50], we assume that the fault normal stress is equal to the overburden. This is a reasonable assumption considering that OTFs are in normal/strike-slip stress state, so the vertical stress (overburden) and maximum horizontal stress are equal. We employ a modified effective pressure law to account for the temperature dependence of viscous creep (Supplementary Information Eqn. 4), which is discussed in detail in the Supplementary Information. In accordance with Byerlee's law[44], μ=0.85 in the shallow crust (P<0.2 GPa) and μ=0.6 at depth. In Fig. 3, we consider conditions of hydrostatic pore pressure (λ=0.4) and friction coefficients for olivine, μ=0.6[4], and serpentine μ=0.1-0.6. The frictional strength of serpentine is dependent on the specific polymorph, slip velocity, and pressure-temperature, so we use a depth-dependent frictional strength based on relevant experimental data[31–33] (see Supplementary Information).

Ductile deformation is represented by a viscoplastic, temperature-dependent flow law similar to Eqn. 1. Depending on the state of the fault zone (protolith or mylonite), the strain rate also depends on water content and grain size. The general form of the flow law for dislocation creep and diffusion creep is:

$$\dot{\varepsilon} = A\sigma^n d^p C_{OH}^r e^{-(E+PV)/RT} \tag{6}$$

in which d is the grain size, p is the grain size exponent, C_{OH} is the water concentration, r is the water concentration exponent, P is pressure, and V is the activation volume. The form of the flow law for low temperature plasticity is:

$$\dot{\varepsilon} = A\sigma^n C_{OH}^r e^{\left[-\frac{E}{RT}\left(1-\frac{\sigma}{\sigma_P}\right)^p\right]^q} \tag{7}$$

where σ_P is the Peierls stress and p and q are non-dimensional parameters that describe dislocation motion. The flow law parameters are provided in Extended Data Table 2.

Methods References

44. Byerlee, J. Friction of rocks. *Pure Appl. Geophys.* **116**, 615–626 (1978).
45. Stein, C. A. & Stein, S. A model for the global variation in oceanic depth and heat flow with lithospheric age. *Nature* **359**, 123–128 (1992).
46. Hartnady, C. J. H. & le Roex, A. P. Southern Ocean hotspot tracks and the Cenozoic absolute motion of the African, Antarctic, and South American plates. *Earth Planet. Sci. Lett.* **75**, 245–257 (1985).
47. Roland, E., Behn, M. D. & Hirth, G. Thermal-mechanical behavior of oceanic transform faults: Implications for the spatial distribution of seismicity. *Geochemistry, Geophys. Geosystems* **11**, 1–15 (2010).
48. Tasaka, M., Hiraga, T. & Zimmerman, M. E. Influence of mineral fraction on the rheological properties of forsterite + enstatite during grain-size-sensitive creep: 2. Deformation experiments. *J. Geophys. Res. Solid Earth* **118**, 3991–4012 (2013).
49. Sibson, R. H. Frictional constraints on thrust, wrench and normal faults. *Nature* **249**, 542–544 (1974).
50. Beeler, N. M., Hirth, G., Thomas, A. & Bürgmann, R. Effective stress, friction, and deep

crustal faulting. *J. Geophys. Res. Solid Earth* **121**, 1040–1059 (2015).

Extended Data

Material properties	
Mantle lithosphere density	3300 kg m^{-3}
Water density	1000 kg m^{-3}
Reference viscosity	1×10^{19} Pa s
Maximum viscosity	1×10^{24} Pa s
Thermal conductivity	3 W m^{-1} K^{-1}
Specific heat	1000 J kg^{-1} K^{-1}
Gas constant	8.3145 J mol^{-1} K^{-1}
Olivine flow law	Dry dislocation creep[18]
Coefficient of friction	0.85
Cohesion	20 MPa
Gravitational acceleration	-9.81 m s^{-2}
Boundary conditions (Shaka)	
Length of fault segment	200 km
Length of ridge segments	50 km
Shaka full spreading rate	12.92 mm yr^{-1}
Surface temperature	0 °C
Mantle potential temperature	1380 °C[39]
Boundary conditions (Gofar)	
Length of fault segment (3)	95 km
Length of ridge segments	50 km / 14 km
Full spreading rate	124.55 mm yr^{-1}
Surface temperature	0 °C
Mantle potential temperature	1300 °C[40]

Extended Data Table 1 | Material properties and boundary conditions for fault thermal models (Fig. 2a-b).

Olivine									
Mechanism	***n***	***p***	***q***	***r***	***A (μm^{-p} s^{-1} MPa^{-n})**	**E (kJ mol^{-1})**	**V (10^{-6} m^3 mol^{-1})**	**σ_p (GPa)**	**Reference**
Dry diffusion creep	1	-3	–	–	1.50E+09	375	2	–	18
	–	–	–	–	3.98E+07	–	–	–	19
Dry GBS	2.9	-0.7	–	–	5.01E+04	445	18	–	19
Dry dislocation creep	3.5	0	–	–	1.10E+05	520	14	–	18
Dry LTP	2	0.5	1	–	1.40E-07	320	0	5.9	41
Wet diffusion creep	1	-3	–	1	4.00E+05	335	4	–	18
Wet GBS	3	-1	–	1.25	1.29E+01	423	17.6	–	20
Wet dislocation creep	3.5	0	–	1.2	3.00E+01	480	11	–	18
Wet LTP	2	0.75	1	–	1.26E+07	518	–	2.1	42
Serpentine									
Mechanism	***n***	***p***	***q***	***r***	**A (μm^{-p} s^{-1} MPa^{-n})**	**E (kJ mol^{-1})**	**V (10^{-6} m^3 mol^{-1})**	**σ_p (GPa)**	**Reference**
Wet dislocation creep	3.8	0	–	–	1.80E-17	8.9	3.2	–	29

Extended Data Table 2 | Flow laws and constitutive parameters used in deformation mechanism maps (Extended Data Figs. 1, 2) and strength-depth profiles (Fig. 3). *The value of A has been adjusted from the original references to account for revised estimates of the water content in the experimental samples[43]. GBS - Grain boundary sliding; LTP - Low temperature plasticity.

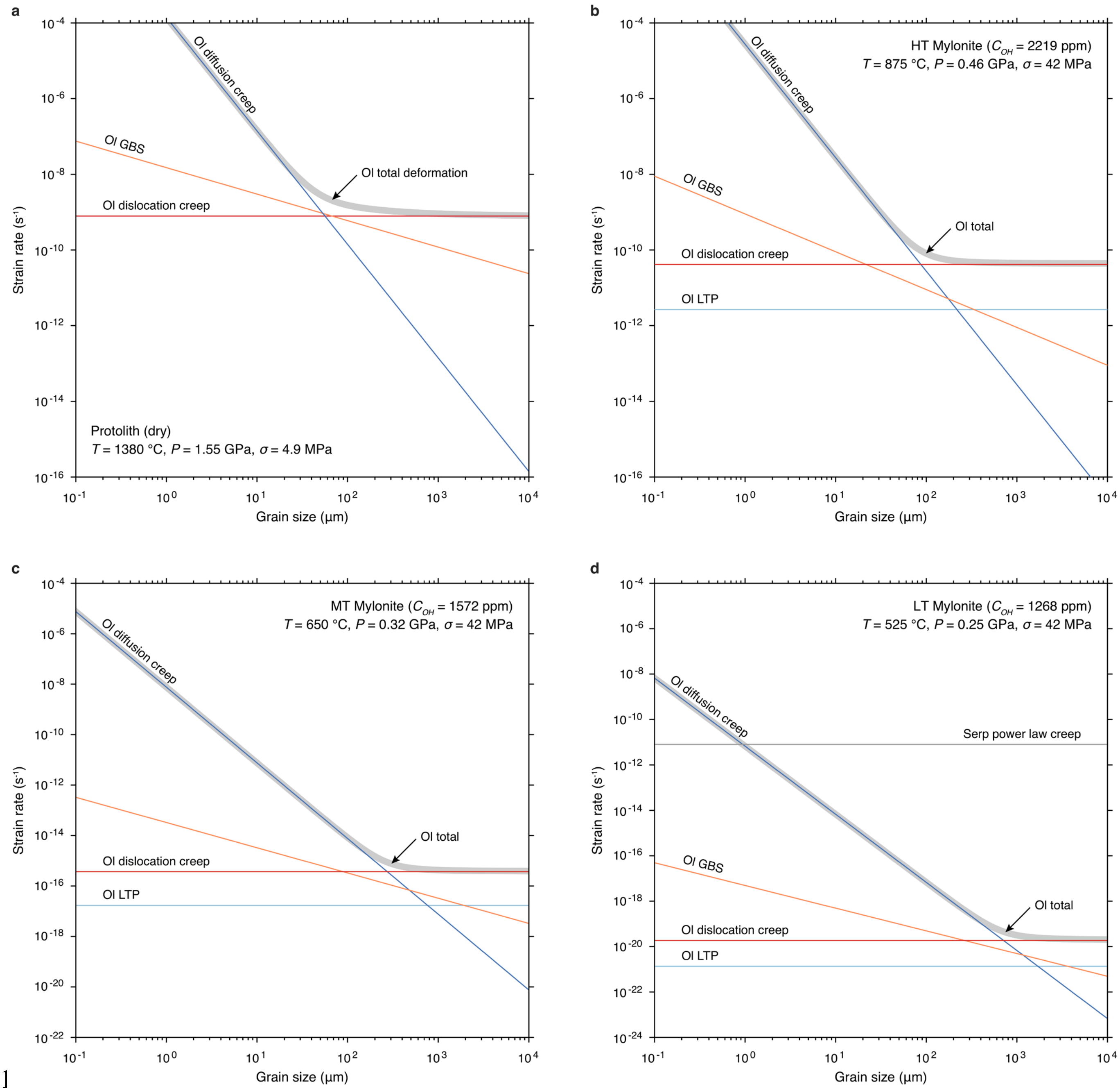

Extended Data Fig. 1 | Deformation mechanism maps for Shaka transform fault calculated using the flow law parameters in Extended Data Table 2. (a) Protolith. (b) HT mylonite. (c) MT mylonite. (d) LT mylonite.

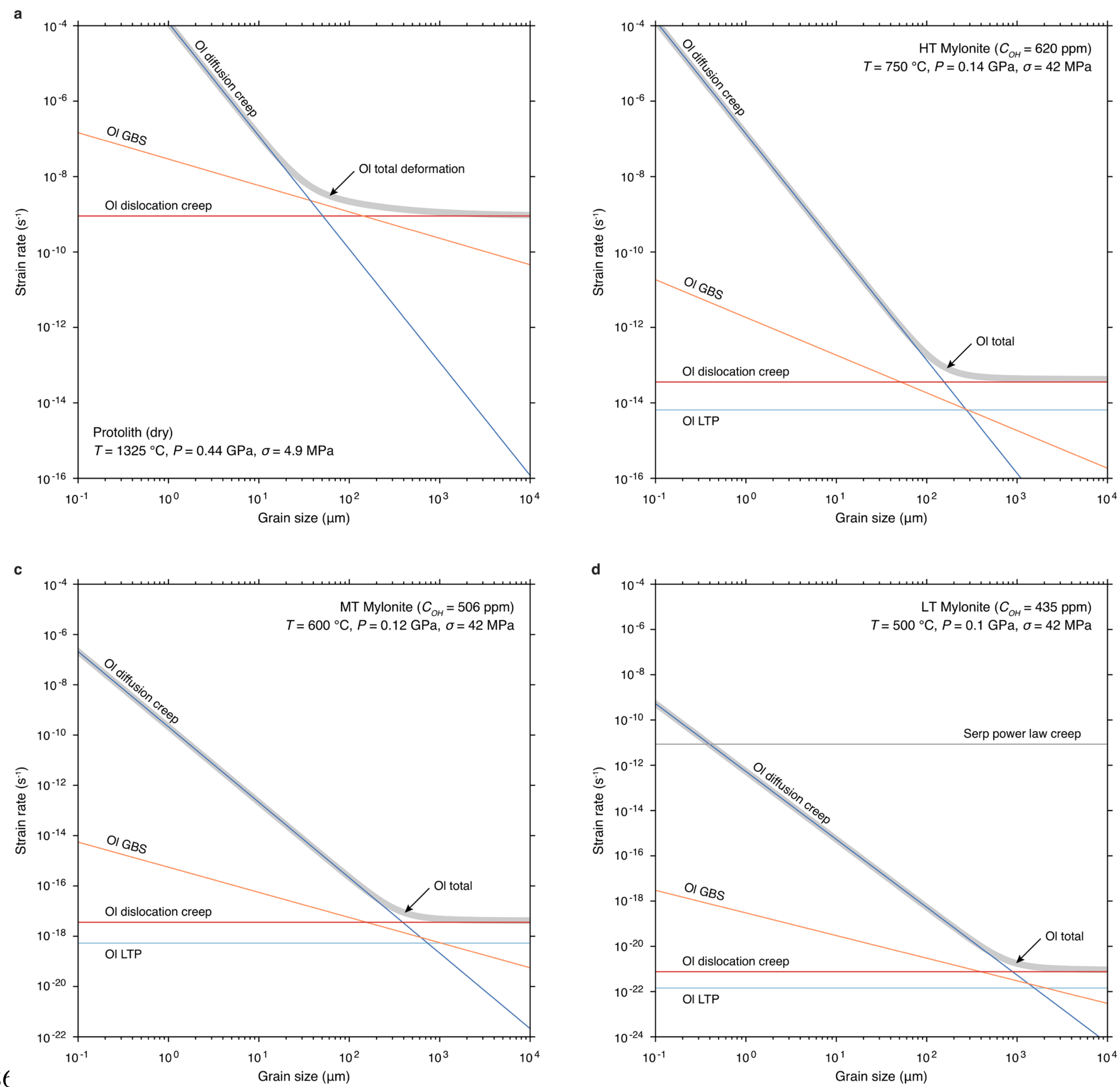

Extended Data Fig. 2 | Deformation mechanism maps Gofar transform fault calculated using the flow law parameters in Extended Table 2. (a) Protolith. (b) HT mylonite. (c) MT mylonite. (d) LT mylonite.

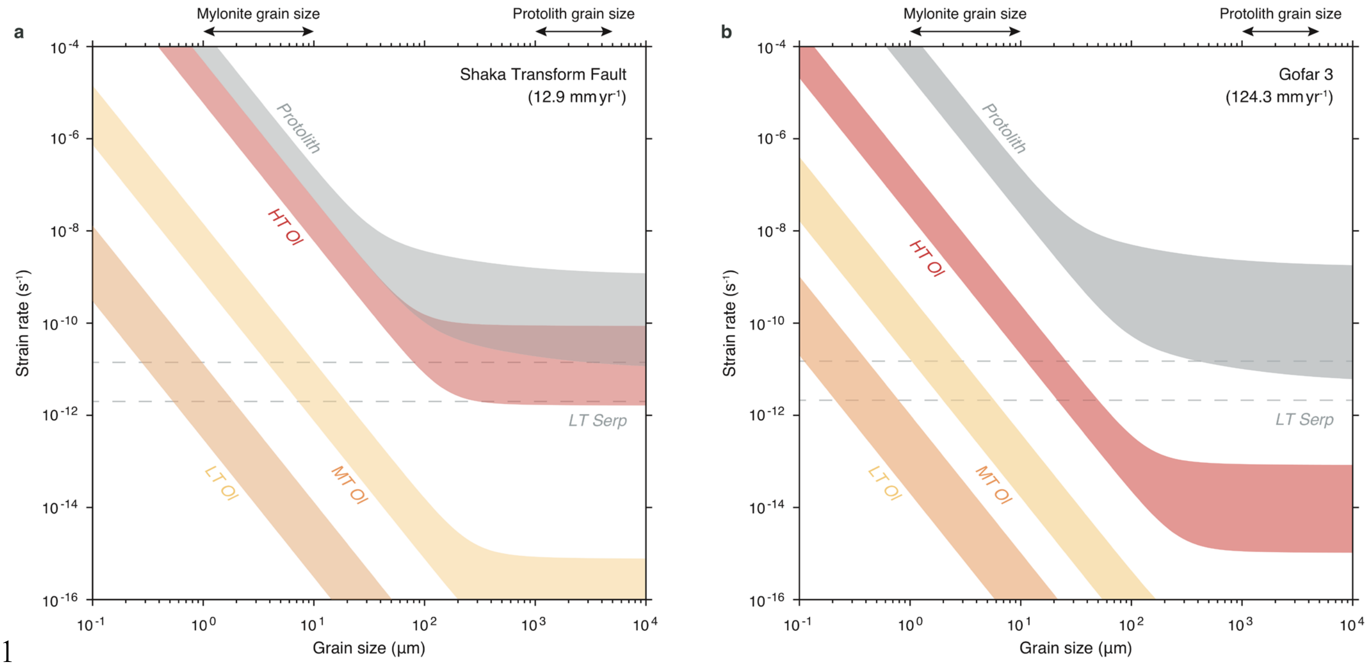

Extended Data Fig. 3 | Composite deformation mechanism maps for (a) Shaka and (b) Gofar transform faults. The total strain rate is the arithmetic sum of the strain rates from each deformation mechanism (i.e., Ol total in Extended Data Figs. 1, 2).

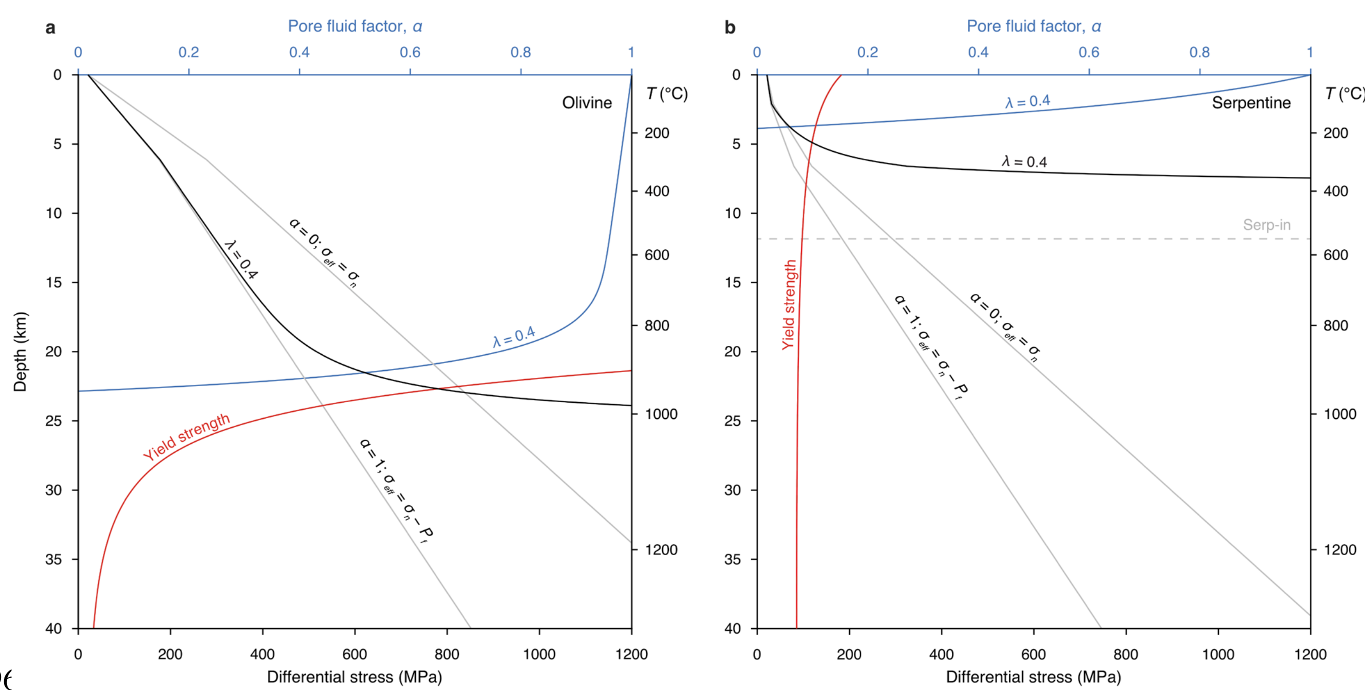

Extended Data Fig. 4 | Modified friction-effective stress relationship for the Shaka transform fault for (a) olivine and (b) serpentine calculated using hydrostatic (λ=0.4) pore pressure. The pore fluid factor, α, decreases from 1 at the surface to 0 at the brittle-ductile transition as the normal stress on asperity contacts nears the yield strength.